ELSEVIER

Contents lists available at ScienceDirect

# **Mechanics of Materials**

journal homepage: www.elsevier.com/locate/mecmat



#### Editor invited article



# Stochastic modeling of spatially-dependent elastoplastic parameters in 316L stainless steel produced by direct energy deposition

Shanshan Chu <sup>a</sup>, Athanasios Iliopoulos <sup>b</sup>, John Michopoulos <sup>b</sup>, John Steuben <sup>b</sup>, James Thomas <sup>c</sup>, Johann Guilleminot <sup>a,\*</sup>

- <sup>a</sup> Department of Civil and Environmental Engineering, Duke University, Durham, NC 27708, USA
- b Computational Multiphysics Systems Lab., Center of Computational Material Science, Naval Research Laboratory, Washington, DC, USA
- <sup>c</sup> Applications of Smart Materials Section, Multifunctional Materials Branch, Naval Research Laboratory, Washington, DC, USA

#### ARTICLE INFO

# ABSTRACT

Keywords:
Stochastic modeling
Elasto-plasticity
Random field
Additive manufacturing
Uncertainty quantification

The stochastic modeling and calibration of an anisotropic elasto-plastic model for additive manufacturing materials are addressed in this work. We specifically focus on 316L stainless steel, produced by directed energy deposition. Tensile specimens machined from two additive manufactured (AM) box-structures were used to characterize material anisotropy and random spatial variations in elasticity and plasticity material parameters. Tensile specimens were cut parallel (horizontal) and perpendicular (vertical) to the AM deposition plane and were indexed by location. These results show substantial variability in both regimes, with fluctuation levels that differ between specimens loaded in the parallel and perpendicular build directions. Stochastic representations for the stiffness and Hill's criterion coefficients random fields are presented next. Information-theoretic models are derived within the class of translation random fields, with the aim of promoting identifiability with limited data. The approach allows for the constitutive models to be generated on arbitrary geometries, using the so-called stochastic partial differential approach (to sampling). These representations are then partially calibrated using the aforementioned experimental results, hence enabling subsequent propagation analyses. Sampling is finally exemplified on the considered structure.

# 1. Introduction

Additive manufacturing (AM), also known as 3D printing, has emerged over the last decade as a promising manufacturing technique for producing complex geometries and customized components with high precision and efficiency (Ian Gibson, 2015). The mechanical behavior of 3D printed materials is significantly influenced by their microstructure, and substantial spatial heterogeneity can be introduced due to complex thermal history and phase evolution during (transient) processing. Such spatial variability translates in spatiallydependent material properties, which can vary significantly along the build direction, across layer interfaces, and within each layer (Huang et al., 2015; Sames et al., 2016; DebRoy et al., 2018). In particular, plasticity-related properties, such as yield strength, ultimate strength, and strain hardening, play a crucial role in determining the (potentially stochastic) mechanical response under external loading. Therefore, the accurate characterization and prediction of elastoplastic parameters in AM materials, including 316L stainless steel, are of great significance for reliable and efficient design and analysis of AM components (Rosa et al., 2018; Prabhune and Suresh, 2020).

Accounting for various types of uncertainties is an important challenge raised by additive manufacturing (Kotha et al., 2020; Mahadevan et al., 2022). Most of the existing works have focused on the propagation of system-parameter uncertainties in AM process modeling (Hu and Mahadevan, 2017; Nath et al., 2017; Wang et al., 2019; Supriyo et al., 2019, 2020) and their impact on macroscale properties (Cai and Mahadevan, 2016), as well as in the integration of model discrepancy (Arendt et al., 2012) using a predictor-corrector approach (see, e.g., Hu and Mahadevan (2017), Nath et al. (2017), Wang et al. (2020)) following the seminal work by Kennedy and O'Hagan (Kennedy and O'Hagan, 2001). Other studies addressed the modeling of stochastic fluctuations in as-built parts, mostly through multiscale-informed strategies that couple microstructure description with a homogenization scheme (Maloth et al., 2020; Ozturk et al., 2021; Weber et al., 2022), or prior representations amenable to direct simulations of random material parameters at coarser mesoscopic scales (Chu et al.,

Invited Editor: Lori Graham-Brady.

\* Corresponding author.

E-mail address: johann.guilleminot@duke.edu (J. Guilleminot).

2021). The former have the benefit of solely relying on an end-to-end computational pipeline that (i) can accommodate any type of constitutive behaviors and (ii) limits modeling bias to microstructure reconstruction. However, they may be intractable when nonstationary effects are pronounced (in which case limited access to microstructure data becomes a limiting factor), or when concurrent coupling becomes too computationally intensive. In contrast, the latter may be more suitable to capture nonstationary effects in the small-data limit, owing to the regularization enabled by the prior model, but typically introduce approximations within classes of (e.g., translation-type) stochastic representations.

The aim of this work is to develop and identify prior models for an anisotropic elastoplastic constitutive model, using physical experiments capturing spatial variations over the printed structure. This unique characterization setting allows us to investigate anisotropy in both material symmetries (for the elastic component) and covariance structure. Attention is restricted to 316L stainless steel produced by direct energy deposition (DED), which is one of the most widely used materials in additive manufacturing due to its excellent mechanical properties and corrosion resistance (Guo and Leu, 2013). Our contributions are as follows:

- We provide and analyze experimental data for both the anisotropic elastic and plasticity properties, investigating anisotropy in terms of both marginal distributions and correlation structures.
- We derive information-theoretic random field models for the elastoplastic constitutive model, using a reduced version of Hill's yield criterion (inferred from processing conditions).
- We propose a methodology to identify model parameters, including hyperparameters in the first-order marginal distributions and spatial correlation lengths.

The rest of this paper is organized as follows. The additive manufacturing and experimental analysis are first presented in Section 2. Section 3 is devoted to stochastic modeling. An overview of the framework is provided, and formulations for both the elasticity and plasticity components are derived. Model calibration is subsequently addressed in Section 4. Concluding remarks are finally provided in Section 5.

# 2. Additive manufacturing process and experiments description

In this section, the additive manufacturing and experimental characterization of a box-shaped structure, made up of 316L stainless steel, are described. Material processing, together with the experimental setup, are first presented in Section 2.1. The experimental results for the tensile tests are then discussed in Section 2.2. In particular, Young's moduli and yield strengths for specimens loaded parallel (horizontal) and perpendicular (vertical) to the AM deposition plane are analyzed.

# 2.1. Description of the experimental setup

Two 316L stainless steel thin-walled boxes (without bottom and top faces) were printed using Directed Energy Deposition (DED), using a Lasertec 65 hybrid manufacturing system; see Fig. 1. Basis of the box is a  $166 \times 166$  [mm] square, height is 130 [mm], and wall thickness is 3 [mm] (see Iliopoulos et al. (2020b) for details). To ensure similar thermal loading during processing, deposition was performed

- clockwise for odd-numbered layers, starting from the lower-lefthand corner of the box; and
- counter-clockwise for the even-numbered layers, starting from the upper-right-hand corner of the box.

After processing, the four faces were collected on each box and eight test samples were harvested on each face, using different cutting directions. Fig. 2 shows the four plates, unfolded from the top of the box, and dashed lines illustrate the correspondence of the bottom corners

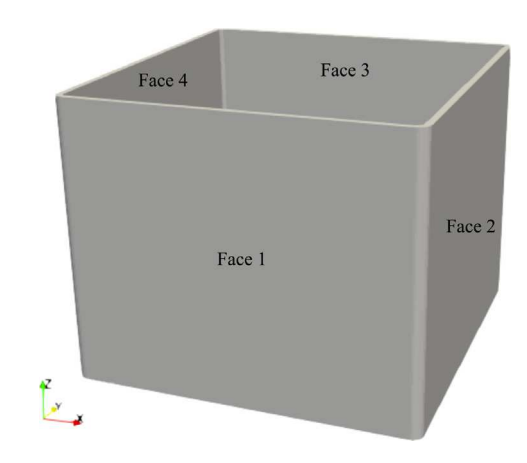
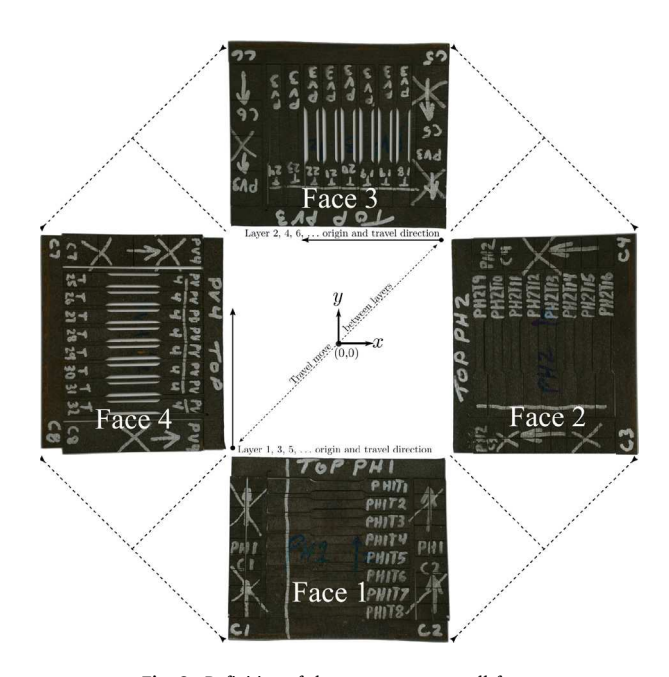


Fig. 1. CAD model of the 3D-printed box, manufactured by Directed Energy Deposition (DED).



**Fig. 2.** Definition of the test coupons on all faces. *Source:* From Iliopoulos et al. (2020b).

of the plates. Starting from the bottom plate, faces are labeled counter-clockwise, with faces numbered from 1 to 4. Cutting directions are also shown in this figure. In particular, Face 1 and Face 2 correspond to specimens that were cut along the in-plane, horizontal direction (along the x-axis for Face 1, and along the y-axis for Face 2), while Faces 3 and 4 have coupons that were cut along the vertical direction (defined by the z-axis). Each box has 32 samples, half of which are associated with either the (x-y) deposit plane or the vertical direction (along z).

Based on the ASTM E8M Standard, subsized (6 mm gage width) "dog-bone" specimens were used. Tensile tests were conducted on an MTS Insight 100 Test System with a 30 [kN] load cell. Specimens were held using 100 [kN] mechanical wedge grips, and the strain was recorded using a video extensometer system. The stress–strain curves for the 64 samples are provided in Fig. 3. It is seen that the yield and ultimate strength stresses for the horizontal samples are generally larger than the ones measured along the vertical directions while the failure elongations are smaller, hence suggesting pronounced anisotropy in terms of strength and ductility. The directional yield stresses also exhibit substantial variability, regardless of the face. This aspect is investigated from a statistical standpoint in the next section.

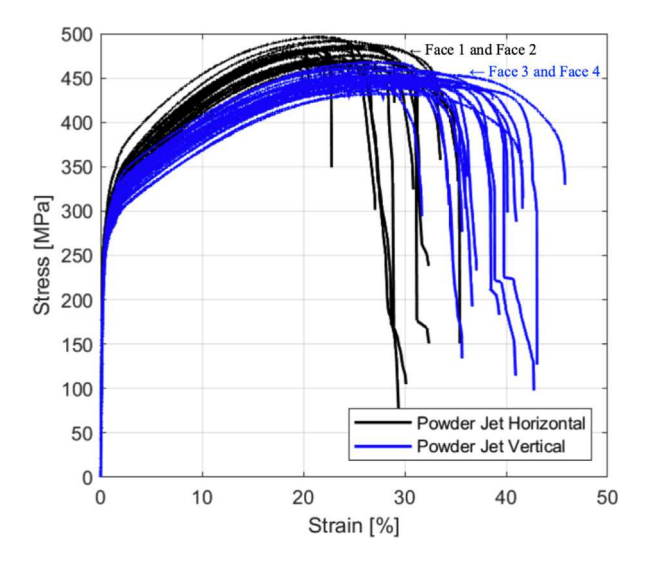


**Fig. 3.** Stress–strain curves obtained for all 64 samples (2 boxes). Black lines correspond to results collected for Faces 1 and 2, while blue lines are associated with Faces 3 and 4, for the two boxes. Observe the variability exhibited by the results, and the fact that horizontal (respectively, vertical) samples have higher strength (respectively, ductility). (For interpretation of the references to color in this figure legend, the reader is referred to the web version of this article.)

Table 1
Samples of the initial yield strength in [MPa] (tensile test, box 1).

Face #	Sample #	Yield strength	Face #	Sample #	Yield strength
	1	255.2	$3~(\bar{\sigma}_{zz})$	17	252.8
	2	264.3		18	253.2
	3	268.8		19	248.3
1 (= )	4	266.1		20	261.1
$1 \ (\bar{\sigma}_{xx})$	5	265.5		21	251.9
	6	255.9		22	249.5
	7	256.0		23	248.0
	8	274.5		24	252.9
2 ( $\bar{\sigma}_{yy}$ )	9	249.4	4 ( $\bar{\sigma}_{zz}$ )	25	264.8
	10	256.9		26	252.0
	11	244.8		27	254.3
	12	250.7		28	256.0
	13	249.8		29	250.2
	14	256.6		30	246.5
	15	273.7		31	253.2
	16	276.6		32	245.6

# 2.2. Experimental results

The realizations of the directional yield stresses extracted from the stress–strain curves (displayed in Fig. 3) are given in Table 1 (box 1) and Table 2 (box 2), respectively. Note that the experimental value for sample #30 (box 2) could not be extracted from the experimental curve properly. The mean values for the yield stress along the x-, y-, and z-axis are estimated to be 266.9149, 256.9128, and 251.9836 [MPa], respectively. The modeling assumption that the behavior is isotropic in the deposit plane is made hereinafter, so that results along the x- and y-axis are merged, which leads to a mean value of 261.9138 [MPa]. The coefficient of variation in the x-y plane is estimated to be 3.68%, which is higher than the coefficient of variation along z, estimated to be 2.17%.

The kernel density estimators (Thompson and Tapia, 1990) estimated with these data are shown in Figs. 4(a) and 4(b). Notice that the probability density function for the yield stress in the vertical direction shows slight bimodality that is indeed generated by two realizations associated with samples located near the boundary of the box.

Table 2
Samples of the initial yield stress in [MPa] (tensile test, box 2).

Face #	Sample #	Yield strength	Face #	Sample #	Yield strength
	1	269.6	3 ( $\bar{\sigma}_{zz}$ )	17	250.0
	2	273.5		18	251.8
	3	276.3		19	258.5
1 (= )	4	272.7		20	266.5
$1 \ (\bar{\sigma}_{xx})$	5	260.9		21	252.8
	6	267.3		22	255.2
	7	266.8		23	250.3
	8	277.0		24	250.5
	9	249.0	4 ( $\bar{\sigma}_{zz}$ )	25	252.0
	10	251.0		26	245.5
	11	251.0		27	243.0
2 (= )	12	254.4		28	250.2
$2 (\bar{\sigma}_{yy})$	13	253.9		29	251.5
	14	260.2		30	\
	15	262.7		31	252.0
	16	269.8		32	241.2

# 3. Definition of Stochastic Hill Elastoplasticity on 3D printed geometries

This section presents the definition of a probabilistic model for the elasto-plastic behavior of AM materials. An overview of the modeling strategy to generate non-Gaussian random fields is first provided in Section 3.1. The construction of the stochastic models for the elastic and plasticity parameters is next presented in Sections 3.2 and 3.3, respectively.

#### 3.1. Overview of the stochastic modeling approach

Let  $\Omega \subset \mathbb{R}^d$ ,  $1 \leq d \leq 3$  be a connected and open domain, with smooth boundary  $\partial \Omega$ . Let  $\{P(x), x \in \Omega\}$  be the second-order random field of material properties which are defined on a probability space  $(\Theta, \mathcal{F}, \mathcal{P})$ :

$$\mathbb{E}\{\|P(x)\|^2\} < +\infty, \quad \forall x \in \Omega, \tag{1}$$

where  $\mathbb{E}$  is the operator of mathematical expectation and  $\|\cdot\|$  is the Euclidean norm. We assume that  $\{P(x), x \in \Omega\}$  takes its values in  $S \subset \mathbb{R}^n$ , where n depends on the quantity of interest;  $2 \le n \le 21$  if P gathers linear elastic parameters (in which case n depends on the material symmetry group), for instance.

Since material properties are typically bounded or semi-bounded, the random field  $\{P(x), x \in \Omega\}$  is non-Gaussian (Guilleminot, 2020). A convenient way to introduce non-Gaussianity while promoting minimal parameterization is to define  $\{P(x), x \in \Omega\}$  as a translation random field (Grigoriu, 1984):

$$P(x) = \mathcal{T}(\Xi(x)), \quad \forall x \in \Omega,$$
 (2)

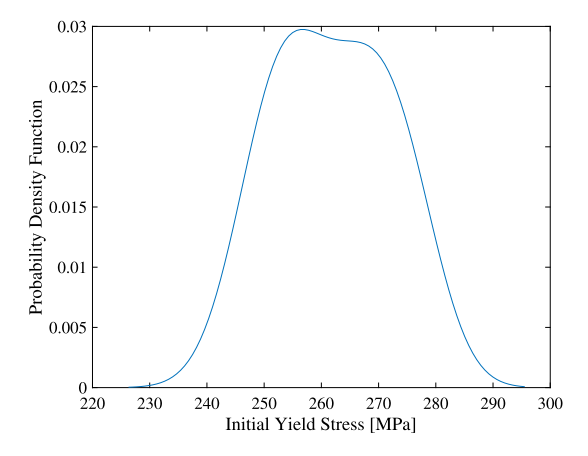
where  $\{\Xi(x), x \in \mathbb{R}^d\}$  is a normalized (that is, centered and with unit marginal variance) Gaussian random field with values in  $\mathbb{R}^n$  and  $\mathcal{T}$  is a measurable mapping such that

$$P(x) \sim \pi$$
, (3)

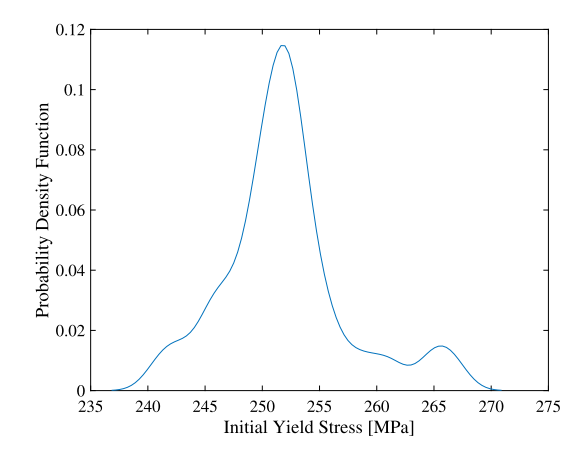
for any x fixed in  $\Omega$ , with  $\pi$  a given probability measure (to be defined momentarily). It is assumed that  $\pi$  admits a probability density function f with respect to the Lebesgue measure  $dp = dp_1 \dots dp_n$  in  $\mathbb{R}^n$ , that is,  $\pi(dp) = f(p) dp$ .

The stochastic modeling of the random field of material parameters then involves two steps:

1. The first step involves the construction of the latent Gaussian random field  $\{\Xi(x), x \in \mathbb{R}^d\}$  and more specifically, its restriction to the complex domain  $\Omega$ .



(a) PDF for the yield stress in the deposit plane



(b) PDF for the yield stress along the z-direction

Fig. 4. Kernel density estimators of the probability density function (PDF) for the yield stress in the deposit plane (left) and along the z-direction (right).

2. The second step is focused on the definition of the transport map  $\mathcal{T}$  (or equivalently, the definition of  $\pi$ ) that pushes forward the standard Gaussian measure to  $\pi$ , at any fixed location in  $\Omega$ .

Methods to address these steps are presented in the next two sections.

#### 3.1.1. Definition of the latent Gaussian field

The challenge of modeling  $\Xi$  on a complex domain  $\Omega$  lies in the fact that the covariance operator can hardly be defined a priori, which makes the use of standard series-based (e.g., Karhunen-Loève) representations impractical. To circumvent this difficulty, we rely on the implicit definition of the *independent* components of the latent vector-valued Gaussian field  $\{\Xi(x), x \in \Omega\}$  as the solution to the following stochastic partial differential equation (SPDE) (Fuglstad et al., 2015):

$$\left(\kappa^2 - \langle \nabla, [H^{(j)}(\mathbf{x})] \nabla \rangle\right)^{\alpha/2} \Xi_j(\mathbf{x}) = \dot{\mathcal{W}}(\mathbf{x}), \quad \mathbf{x} \in \mathbb{R}^d, \tag{4}$$

where  $\kappa$  is a model parameter,  $\langle \cdot, \cdot \rangle$  is the Euclidean inner product in  $\mathbb{R}^d$ ,  $\nabla$  is the nabla (del) operator, [H] is a diffusion field,  $\alpha = \nu + d/2$ (with  $\nu$  the smoothness parameter in the associated Matérn covariance function), and  $\{\dot{\mathcal{W}}(x), x \in \mathbb{R}^d\}$  is the normalized Gaussian white noise. The isotropic counterpart of Eq. (4) was originally considered in Whittle (1954, 1963), and regained attraction recently due to the seminal work by Lindgren et al. (2011) that described an efficient numerical strategy to solve the SPDE; see Roininen et al. (2014), Dunlop and Stuart (2016), Sidén et al. (2017), Roininen et al. (2019), Sidén et al. (2019), Mejia et al. (2020), Bolin and Lindgren (2011), Staber and Guilleminot (2017), Guilleminot et al. (2019), Staber and Guilleminot (2018), Chu and Guilleminot (2019), Bolin and Kirchner (2020), Bolin and Wallin (2020), Chu et al. (2021) for various applications, as well as (Lindgren et al., 2022) for a review. In practice, solving Eq. (4) on the bounded domain  $\Omega$  requires the choice of appropriate boundary conditions. While the use of homogeneous Neumann boundary conditions was invoked in Lindgren et al. (2011) to simplify the weak form obtained in the Galerkin setting, other boundary conditions were explored in Roininen et al. (2014), Daon and Stadler (2018), Khristenko et al. (2019) to circumvent boundary effects on the marginal variance and covariance structure. The above formulation is particularly well adapted to sampling on complex domains, owing to the capability of capturing features through an ad hoc definition of the diffusion

$$[H^{(j)}(x)] = \sum_{i=1}^{d} \lambda_i^{(j)} e^{(i)}(x) \otimes e^{(i)}(x), \quad \forall \, x \in \Omega,$$
 (5)

where the set of coefficients  $\{\lambda_i^{(j)}\}_{i=1}^d$  controls the correlation lengths in the covariance function of the latent Gaussian field  $\{\Xi_j(\mathbf{x}), \mathbf{x} \in \Omega\}$ ,  $1 \leq j \leq n$ , and the orientation, or directional, fields  $\{\mathbf{x} \mapsto e^{(i)}(\mathbf{x})\}_{i=1}^d$ 

enforce directions of local noise filtering. Considering deposition paths for the definition of these orientation fields provides a path towards the seamless integration of processing conditions within the stochastic modeling framework. In the case laser trajectory cannot be tracked during manufacturing, these fields can alternatively be defined by introducing application-dependent fictitious flow problems (Staber and Guilleminot, 2017; Guilleminot et al., 2019; Staber and Guilleminot, 2018; Chu and Guilleminot, 2019; Chu et al., 2021). Specifically, each field is here defined as

$$e^{(i)}(x) = \frac{1}{\|\nabla \Psi_i(x)\|} \nabla \Psi_i(x) , \quad \forall x \in \Omega, \quad 1 \le i \le d,$$
 (6)

where  $\Psi_i$  is the solution to the Laplace equation

$$\Delta \Psi(\mathbf{x}) = 0, \quad \forall \, \mathbf{x} \in \Omega. \tag{7}$$

The key idea is then to supplement the above equation with problemand field-specific Dirichlet boundary conditions that drive the flow along desired paths, as well as with Neumann boundary conditions that enforce the normal component of the flow velocity to vanish at interfaces with geometrical features. This construction will be exemplified in Section 4.3.

# 3.1.2. Construction of the transport map

The definition of the transport map  $\mathcal{T}$  can be achieved in various ways, ranging from the simple use of empirical cumulative distribution functions (CDFs), estimated from the data, to selection within a set of admissible transformations—which are those compatible with the information available on the considered material parameters (such as boundedness). On the one hand, the use of empirical CDFs raises estimator convergence issues when the number of samples is not large enough. Additionally, it does not ensure that the aforementioned information is satisfied (almost surely). On the other hand, arbitrary model selection increases bias and may thus be detrimental to the uncertainty analysis. In this work, we invoke information theory (Jaynes, 1957b,a) and more specifically, the principle of maximum entropy, as a means to construct f objectively. Assume that the constraint

$$\mathbb{E}\{\Phi(P(x))\} = \phi \tag{8}$$

represents some available information, where  $\Phi$  is a vector-valued mapping encoding the information available on P(x) (with x fixed in  $\Omega$ ) and  $\phi$  is a given vector. For instance, taking  $\Phi$  as the identity function indicates that the mean value of P(x) is given (by  $\phi$ , in this case). Similarly, defining  $\Phi$  as  $\Phi(p) = \text{vec}(p \otimes p)$ , where "vec" represents the vectorization function, implies that the correlation matrix of P(x) is known (and given, in vectorized form, by  $\phi$ ). The probability density

function induced by the principle of maximum entropy is then defined as

$$f = \arg\max_{g \in C} H\{g\},\tag{9}$$

where  $C_{\pi}$  represents the set of admissible functions that satisfy the constraints given by Eq. (8) and  $H\{g\}$  is the so-called Shannon's entropy of g (see Shannon (1948a,b)):

$$H\{g\} = \int_{S} g(\boldsymbol{p}) \ln (g(\boldsymbol{p})) d\boldsymbol{p}, \qquad (10)$$

where S is the support of f. The solution to the above optimization problem is easily obtained using the method of Lagrange multipliers and reads as

$$f(\mathbf{p}) = I_{\mathcal{S}}(\mathbf{p}) \times c \times \exp\{-\langle \Lambda, \Phi(\mathbf{p}) \rangle\}, \tag{11}$$

where  $I_S$  is the indicator function of S, c is the normalization constant, and  $\Lambda$  is the (vector-valued) Lagrange multiplier. Note that while this strategy is a classical approach for constructing prior models in Bayesian inference and offers the benefit of reducing modeling bias, it is not claimed, by no means, that the model thus obtained is the ground truth. It is, however, fully consistent with the mathematical properties that are required to ensure well-posedness in the forward propagation problem, and allows for calibration using a limited amount of data (due to its low-dimensional parameterization).

In the following, we invoke the information-theoretic framework to construct stochastic models for the elasticity and plasticity parameters (see Sections 3.2.2 and 3.3.2, respectively). Since no cross-information can be introduced between these parameters, it follows that

$$\pi = \pi_{\mathcal{E}} \otimes \pi_{\mathcal{P}} \,, \tag{12}$$

where  $\pi$  is the joint probability distribution for the elasticity and plasticity parameters, and  $\pi_{\mathcal{E}}$  and  $\pi_{\mathcal{D}}$  are the marginal probability distributions for these parameters. The construction can therefore be completed independently for the two families of material parameters. Hereinafter, the notation P(x) is therefore used as a generic variable to refer to any set of material parameters (i.e., either elasticity or plasticity parameters).

## 3.2. Stochastic elasticity formulation

#### 3.2.1. Preliminaries

We first consider the stochastic modeling of the elasticity tensor. The information-theoretic modeling of elasticity fields has attracted much attention over the last two decades, starting from the seminal work by Soize for purely anisotropic materials (that is, with values in the triclinic symmetry class) (Soize, 2006) to the latest unified results for all symmetry classes presented in Staber and Guilleminot (2017); see Guilleminot (2020) for a review, as well as (Acton and Baxter, 2018) for use in a mesoscale modeling setting and Ostoja-Starzewski (2007) for an introduction to stochastic multiscale mechanics.

Let [C(x)] be the random matrix representation (in Voigt form) of the stochastic fourth-order elasticity tensor. Based on processing conditions, and for a given x fixed in  $\Omega$ , we assume that the elasticity tensor takes values in the set  $\mathbb{M}^{\text{ti}}(n(x))$  of transversely isotropic tensors, where n(x) is the unit vector defining the symmetry group at  $x \in \Omega$ . For instance, we take  $n(x) = (1,0,0)^T$  on faces 1 and 3, while  $n(x) = (0,1,0)^T$  on faces 2 and 4. In order to ensure well-posedness, the regularization

$$[C(\mathbf{x})] = \frac{1}{1+\epsilon} [\underline{C}]^{1/2} \{ \epsilon [I_6] + [\mathbf{M}(\mathbf{x})] \} [\underline{C}]^{1/2}, \quad \forall \mathbf{x} \in \Omega,$$
(13)

is first introduced to recover a uniform coercivity condition, where  $[\underline{C}] = \mathbb{E}\{[C(x)]\}$  and  $0 < \epsilon \ll 1$  (Nouy and Soize, 2014). In the above equation,  $\{[M(x)], x \in \Omega\}$  is an auxiliary, normalized elasticity field with values in  $\mathbb{M}^{\mathrm{ti}}(n(x))$  such that

$$\mathbb{E}\{[\boldsymbol{M}(\boldsymbol{x})]\} = [I_6], \quad \forall \boldsymbol{x} \in \Omega, \tag{14}$$

by construction. Notice that the above equation takes the form of a mathematical expectation and can therefore be accounted for in the principle of maximum entropy. In addition, it is necessary to add another constraint to ensure the well-posedness of the associated stochastic boundary value problem. Following the methodology proposed in Soize (2006), this can be achieved by considering the additional constraint

$$\mathbb{E}\{\log\left(\det([\boldsymbol{M}(\boldsymbol{x})])\right)\} = \zeta, \quad |\zeta| < +\infty, \tag{15}$$

in which the right-hand is taken as constant without loss of generality. The next methodological step then consists in expanding the normalized field as

$$[\mathbf{M}(\mathbf{x})] = \sum_{i=1}^{5} M_i(\mathbf{x}) [E_i(\mathbf{x})],$$
 (16)

where  $\{M_i(x), x \in \Omega\}$ ,  $1 \le i \le 5$ , are scalar-valued random fields and  $\{[E_i(x)]\}_{i=1}^5$  constitutes the Walpole basis of  $\mathbb{M}^{\text{ti}}(n(x))$  in Voigt form (Walpole, 1984). The tensor basis writes

$$[[E_1(x)]] = [P(x)] \otimes [P(x)], \quad [[E_2(x)]] = ([Q(x)] \otimes [Q(x)])/2,$$
$$[[E_3(x)]] = ([P(x)] \otimes [Q(x)] + [Q(x)] \otimes [P(x)])/\sqrt{2},$$

 $\llbracket E_5(x) \rrbracket = [P(x)] \boxtimes [Q(x)] + [Q(x)] \boxtimes [P(x)],$ 

where

$$[P(x)] = n(x) \otimes n(x), \quad [Q(x)] = [I_3] - [P(x)] \tag{18}$$

and the symbol  $\boxtimes$  denotes the symmetric tensor product between second-order tensors, defined as  $([U] \boxtimes [V])_{ijkl} = (U_{ik}V_{jl} + U_{il}V_{jk})/2$ , with  $(\mathbf{a} \otimes \mathbf{b})_{ij} = a_i b_j$  for any vectors  $\mathbf{a}$  and  $\mathbf{b}$ , and  $([A] \otimes [B])_{ijkl} = A_{ij}B_{kl}$  for any second-order tensors [A] and [B].

The representation in Eq. (16) can be reorganized in the form of a symbolic representation that reflects the structure of the space  $\mathbb{M}^{\mathrm{ti}}(n(x))$ :

$$[\mathbf{M}(\mathbf{x})] = \{ [\mathbf{N}(\mathbf{x})], M_4(\mathbf{x}), M_5(\mathbf{x}) \},$$
 (19)

with

$$[N(x)] = \begin{bmatrix} M_1(x) & M_3(x) \\ M_3(x) & M_2(x) \end{bmatrix}.$$
 (20)

#### 3.2.2. Information-theoretic stochastic model for the elasticity tensor

It was shown in Staber and Guilleminot (2017) that the information introduced in Section 3.2.1, given by Eq. (14)–(15), can be transferred to the elements in the symbolic representation defined in Eq. (19). This equivalence implies that

$$\mathbb{E}\{[N(x)]\} = [I_2], \quad \mathbb{E}\{M_4(x)\} = 1, \quad \mathbb{E}\{M_5(x)\} = 1, \quad \forall x \in \Omega, \quad (21)$$

together with

$$\mathbb{E}\{\log\left(\det([N(x)])\right)\} = \zeta_{123}\,, \quad |\zeta_{123}| < +\infty\,, \tag{22}$$

and

$$\mathbb{E}\{\log\left(M_4(\mathbf{x})\right)\} = \varsigma_4, \quad |\varsigma_4| < +\infty, \quad \mathbb{E}\{\log\left(M_5(\mathbf{x})\right)\} = \varsigma_5, \quad |\varsigma_5| < +\infty.$$
(23)

Since the above constraints do not contain cross-information, it can be deduced that

$$\pi_{\mathcal{E}} = \pi_N \otimes \pi_{M4} \otimes \pi_{M5} \,, \tag{24}$$

with obvious notation. Using the first equation in Eqs. (21) and (22), it is found that the random matrix [N(x)] belongs to the set SG<sup>+</sup> of random matrices constructed in Soize (2000), and is thus defined by the following probability density function:

$$p_{[N(\mathbf{x})]}([n]) = \mathbb{1}_{\mathbb{R}_{>0}^{2\times 2}}([n]) c \left(\det([n])\right)^{3(1-\delta_{[N]}^2)/(2\delta_{[N]}^2)} \exp\left(-\frac{3}{2\delta_{[N]}^2} \operatorname{tr}([n])\right),$$
(25)

where c is the normalization constant. In the above equation,  $\delta_{[N]}$  denotes the coefficient of variation of [N(x)]:

$$\delta_{[N]} = \left\{ \frac{1}{2} \mathbb{E}\{\|[N(x)] - [I_2]\|_F^2\} \right\}^{1/2}.$$
 (26)

Notice that  $\delta_{[N]}$  is spatially-varying when the right-hand side in Eq. (22) depends on location. Following Soize (2000, 2006), the random matrix [N(x)] can then be written as

$$[N(x)] = [L(x)]^{T} [L(x)], (27)$$

where for x fixed in  $\Omega$ , [L(x)] is an upper-triangular random matrix, the components of which are defined as

$$L_{11}(\mathbf{x}) = \frac{\delta_{[N]}}{\sqrt{3}} \sqrt{2F_{\mathcal{G}(\frac{3}{2\delta_{[N]}^2},1)}^{-1} (F_{\mathcal{N}(0,1)}(\Xi_1(\mathbf{x})))},$$
 (28)

$$L_{22}(\mathbf{x}) = \frac{\delta_{[N]}}{\sqrt{3}} \sqrt{2F_{\mathcal{G}(\frac{3}{2\delta_{[N]}^2} - \frac{1}{2}, 1)}^{-1} (F_{\mathcal{N}(0,1)}(\Xi_2(\mathbf{x})))}},$$
 (29)

$$L_{12}(\mathbf{x}) = \frac{\delta_{[N]}}{\sqrt{3}} \Xi_4(\mathbf{x}). \tag{30}$$

Using the second and third equations in Eq. (21), as well as Eq. (23), it is found that  $\{M_4(x), x \in \Omega\}$  and  $\{M_5(x), x \in \Omega\}$  are marginally Gamma distributed and can thus be defined as

$$M_4(\mathbf{x}) = F_{G(a_4,b_4)}^{-1}(F_{\mathcal{N}(0,1)}(\Xi_4(\mathbf{x}))),$$
(31)

and

$$M_5(\mathbf{x}) = F_{G(a_5, h_5)}^{-1}(F_{\mathcal{N}(0,1)}(\Xi_5(\mathbf{x}))), \tag{32}$$

where  $(a_4, b_4)$  and  $(a_5, b_5)$  are the pairs of shape and scale parameters in the Gamma law associated with  $M_4$  and  $M_5$ , respectively.

# 3.3. Stochastic plasticity formulation

# 3.3.1. Deterministic plasticity modeling

In this work, the 3D-printed material characterized in Section 2 is described using Hill's yield criterion. In the case where the axes (x,y,z) coincide with the axes of orthotropy, the Hill yield function is expressed by

$$f([\sigma]) = F(\sigma_{yy} - \sigma_{zz})^2 + G(\sigma_{zz} - \sigma_{xx})^2 + H(\sigma_{xx} - \sigma_{yy})^2 + 2L\sigma_{yz}^2 + 2M\sigma_{zx}^2 + 2N\sigma_{xy}^2 - 1,$$
(33)

where F, G, H, L, M, and N are Hill's constants. The latter are related to yield and ultimate shear stresses, denoted by  $(\bar{\sigma}_{xx}, \bar{\sigma}_{yy}, \bar{\sigma}_{zz})$  and  $(\bar{\sigma}_{xy}, \bar{\sigma}_{xz}, \bar{\sigma}_{yz})$ , respectively, by the following equations:

$$F = \frac{1}{2} \left( \frac{1}{\bar{\sigma}_{yy}^2} + \frac{1}{\bar{\sigma}_{zz}^2} - \frac{1}{\bar{\sigma}_{xx}^2} \right), G = \frac{1}{2} \left( \frac{1}{\bar{\sigma}_{zz}^2} + \frac{1}{\bar{\sigma}_{xx}^2} - \frac{1}{\bar{\sigma}_{yy}^2} \right),$$

$$H = \frac{1}{2} \left( \frac{1}{\bar{\sigma}_{xx}^2} + \frac{1}{\bar{\sigma}_{yy}^2} - \frac{1}{\bar{\sigma}_{zz}^2} \right),$$

$$L = \frac{1}{2(\bar{\sigma}_{yz})^2}, M = \frac{1}{2(\bar{\sigma}_{xz})^2}, N = \frac{1}{2(\bar{\sigma}_{xy})^2}.$$
(34)

Note that the yield function in Eq. (33) can also be expressed in terms of reference yield and ultimate shear stresses, in which case Hill's constants are replaced by dimensionless material parameters.

Adopting a standard Voigt representation for stresses, defined as

$$\sigma = (\sigma_{xx}, \sigma_{yy}, \sigma_{zz}, \sigma_{yz}, \sigma_{xz}, \sigma_{yz})^T, \tag{35}$$

the yield function reads as

$$f(\sigma) = \sigma^{T}[A]\sigma - 1, \tag{36}$$

where [A] is the symmetric matrix given by

$$[A] = \begin{bmatrix} G+H & -H & -G & 0 & 0 & 0 \\ -H & F+H & -F & 0 & 0 & 0 \\ -G & -F & F+G & 0 & 0 & 0 \\ 0 & 0 & 0 & 2L & 0 & 0 \\ 0 & 0 & 0 & 0 & 2M & 0 \\ 0 & 0 & 0 & 0 & 0 & 2N \end{bmatrix}.$$
(37)

Since the behavior and microstructural features are found to be similar along the x and y axes in the experiments, it is assumed that  $\bar{\sigma}_{xx} = \bar{\sigma}_{yy}$  and  $\bar{\sigma}_{yz} = \bar{\sigma}_{xz}$  (Iliopoulos et al., 2020a). Under these assumptions, the yield criterion can be simplified to

$$f([\sigma]) = U[(\sigma_{yy} - \sigma_{zz})^2 + (\sigma_{zz} - \sigma_{xx})^2] + V(\sigma_{xx} - \sigma_{yy})^2 + 2M(\sigma_{yz}^2 + \sigma_{xz}^2) + 2N\sigma_{xy}^2 - 1,$$
(38)

where U and V are the material parameters defined as

$$U = \frac{1}{2(\bar{\sigma}_{zz})^2}, \quad V = \frac{1}{(\bar{\sigma}_{xx})^2} - \frac{1}{2(\bar{\sigma}_{zz})^2}.$$
 (39)

Since the ultimate shear stresses could not be characterized in the experiments, the standard assumptions  $\bar{\sigma}_{yz} = \bar{\sigma}_{xz} / \sqrt{3}$  and  $\bar{\sigma}_{xy} = \bar{\sigma}_{xx} / \sqrt{3}$  (obtained by requiring the criterion to coincide with the von Mises stress in the isotropic case) are retained, so that [A] finally reads as

$$[A] = \begin{bmatrix} U+V & -V & -U & 0 & 0 & 0 \\ -V & U+V & -U & 0 & 0 & 0 \\ -U & -U & 2U & 0 & 0 & 0 \\ 0 & 0 & 0 & 6U & 0 & 0 \\ 0 & 0 & 0 & 0 & 6U & 0 \\ 0 & 0 & 0 & 0 & 0 & 3(U+V) \end{bmatrix}. \tag{40}$$

The construction of a probabilistic model for the material parameters U and V is addressed in the next section.

3.3.2. Information-theoretic stochastic model for reduced Hill's coefficients In this section, we consider the stochastic modeling of the reduced Hill's coefficients U and V, viewed as random fields. We, therefore, introduce the random field of plasticity parameters  $\{(U(x),V(x))^T,x\in\Omega\}$ , defined on a given probability space. Following the methodology presented in Section 3, a translation model is introduced as

$$(U(\mathbf{x}), V(\mathbf{x}))^T = \mathcal{T}(\Xi(\mathbf{x})), \quad \forall \, \mathbf{x} \in \Omega.$$
(41)

To construct the pushforward transformation  $\mathcal{T}$ , we observe that constraints related to the definition of [A] (see Section 3.3.1) write

$$U > 0, \quad U + V > 0.$$
 (42)

It is thus convenient to introduce the random field  $\{W(x), x \in \Omega\}$ , with

$$W(\mathbf{x}) = U(\mathbf{x}) + V(\mathbf{x}), \tag{43}$$

so that the stochastic model can be defined on  $\{P(x) = (U(x), W(x))^T, x \in \Omega\}$ . In this case, the transport map can be defined by imposing

$$\mathbb{E}\{P(x)\} = p \tag{44}$$

and

$$|\mathbb{E}\{\log P_i(\mathbf{x})\}| < +\infty, \quad i = 1, 2, \tag{45}$$

with

$$P_i(\mathbf{x}) > 0, \quad i = 1, 2.$$
 (46)

Note that these constraints also imply that both  $\bar{\sigma}_{xx}(x)$  and  $\bar{\sigma}_{zz}(x)$  are second-order random variables,  $\forall x \in \Omega$ , and that the consideration of additional information (e.g., the existence of an upper bound) would lead to other probability distributions (e.g., a truncated Gaussian distribution; see Pokusiński and Kamiński (2023) for an example, as well

Table 3
Samples of the horizontal Young's modulus in [GPa] (tensile test)

Batch #	Sample #	$E_{\ell}$ [GPa]	Batch #	Sample #	$E_{\ell}$ [GPa]
	1	131	3	17	124
	2	122		18	137
	3	132		19	153
1	4	130		20	126
1	5	110		21	129
	6	112		22	136
	7	118		23	139
	8	114		24	122
	9	112	4	25	112
	10	128		26	94.5
	11	109		27	96.0
0	12	108		28	119
2	13	117		29	123
	14	113		30	123
	15	128		31	109
	16	124		32	129

as Kamiński (2021) for yet another way to use the maximum entropy principle). This case is formally analogous to the one presented in Section 3.1.1, which leads us to consider

$$\pi_{\mathcal{P}} = \pi_U \otimes \pi_W \tag{47}$$

with obvious notation, where

$$P_{1}(\mathbf{x}) = F_{\mathcal{G}(1/\delta_{T}^{2}, \underline{u}\delta_{T}^{2})}^{-1} \left( F_{\mathcal{N}(0,1)} \left( \Xi_{1}(\mathbf{x}) \right) \right), \quad \forall \mathbf{x} \in \Omega,$$

$$(48)$$

and

$$P_{2}(\mathbf{x}) = F_{\mathcal{G}(1/\delta_{W}^{2}, \underline{w}\delta_{W}^{2})}^{-1} \left( F_{\mathcal{N}(0,1)} \left( \Xi_{2}(\mathbf{x}) \right) \right), \quad \forall \mathbf{x} \in \Omega,$$

$$\tag{49}$$

where the hyperparameters were expressed in terms of the mean values  $\underline{u}$  and  $\underline{w}$ , and coefficients of variations  $\delta_U$  and  $\delta_W$ . Note that U(x) and V(x) are statistically dependent owing to the change of variables.

**Remark 1.** Following Hun et al. (2019), cross-correlation between the plasticity parameters can be introduced through the transport maps

$$P_{1}(\mathbf{x}) = \left(F_{\mathcal{C}(1/\delta_{U}^{2},\underline{u}\delta_{U}^{2})}^{-1} \circ F_{\mathcal{N}(0,1)}\right) \left(\Xi_{1}(\mathbf{x})\right), \quad \forall \mathbf{x} \in \Omega,$$

$$(50)$$

and

$$P_{2}(\boldsymbol{x}) = \left(F_{\mathcal{G}(1/\delta_{W}^{2},\underline{w}\delta_{W}^{2})}^{-1} \circ F_{\mathcal{N}(0,1)}\right) \left(\rho_{UW}\Xi_{1}(\boldsymbol{x}) + \sqrt{1 - \rho_{UW}^{2}}\Xi_{2}(\boldsymbol{x})\right), \quad \forall \boldsymbol{x} \in \Omega,$$

$$(51)$$

where  $\rho_{UW} \in [-1,1]$  is the Pearson correlation coefficient between U and W. In practice, it is useful to express some of the above statistical parameters in terms of the ones associated with U(x) and V(x). Denoting by  $\underline{v}$  and  $\delta_V$  the mean and coefficient of variation of V(x), and using "sd" to denote the standard deviation, it follows from straightforward algebra that

$$\delta_W = \frac{1}{w} \sqrt{2 \operatorname{sd}_U \left( \operatorname{sd}_U + \rho_{UV} \operatorname{sd}_V \right) + \operatorname{sd}_V^2 - \operatorname{sd}_U^2}$$
 (52)

and

$$\rho_{UW} = \frac{\operatorname{sd}_{U}^{2} + \rho_{UV}\operatorname{sd}_{U}\operatorname{sd}_{V}}{\operatorname{sd}_{U}\operatorname{sd}_{W}},$$
(53)

where  $\mathrm{sd}_W = \underline{w} \delta_W$ ,  $\rho_{UV}$  is the (target) Pearson correlation coefficient between U(x) and V(x), and use was made of the equality  $\mathrm{Var}(V) = \mathrm{Var}(W-U) = \mathrm{Var}(W) - 2\mathrm{Cov}(W,U) + \mathrm{Var}(U)$ . In the present work, such cross-correlation is not introduced due to data limitation, given that the directional yield stresses are not characterized at the same location (hence leaving  $\rho_{UV}$ , or equivalently  $\rho_{UW}$ , undetermined).

**Table 4**Samples of the transverse Young's modulus in [GPa] (tensile test).

Batch #	Sample #	$E_t$ [GPa]	Batch #	Sample #	$E_t$ [GPa]
	1	108	3	17	109
	2	112		18	102
	3	107		19	102
1	4	112		20	0.985
1	5	120		21	102
	6	108		22	108
	7	118		23	117
	8	105		24	108
	9	127	4	25	114
	10	104		26	124
	11	104		27	104
2	12	109		28	108
2	13	104		29	115
	14	102		30	\
	15	102		31	101
	16	111		32	121

#### 4. Model calibration and simulations

We first address, in Section 4.1, the calibration of the parameters in the first-order marginal distribution for the elasticity and plasticity models. We next identify, in Section 4.2, some of the spatial correlation lengths for the plasticity model. Sampling is finally illustrated with the calibrated model in Section 4.3.

# 4.1. Calibration of first-order marginal distribution

# 4.1.1. Stochastic elasticity model

Following the formulation presented in Section 3.2, we seek to calibrate the mean model and coefficients of variation defining the first-order marginal distribution. The correlation lengths for the latent Gaussian random fields cannot be estimated due to data limitation (which raises non-uniqueness issues given that the Walpole components are not directly observed). The database consists of samples of restrictions of the random fields, namely

- $\{E_{\ell}(0, -L_{12}/2, x_3), x_3 \in \Omega_3\}$ , characterized on Face 1;
- $\{E_{\ell}(L_{12}/2,0,x_3), x_3 \in \Omega_3\}$ , characterized on Face 2;
- $\{E_t(x_1, L_{12}/2, L_3/2), x_1 \in \Omega_1\}$  characterized on Face 3;
- $\{E_t(-L_{12}/2, x_2, L_3/2), x_2 \in \Omega_2\}$  characterized on Face 4;

where  $E_{\ell}$  and  $E_t$  are the horizontal and vertical Young's moduli, indexing domains  $\{\Omega_i\}_{i=1}^3$  are defined with respect to faces (see Fig. 2), and  $L_{12}=166$  [mm] and  $L_3=130$  [mm] are the width and height of the box. The realizations extracted from the stress–strain curves shown in Fig. 3 are provided in Tables 3 and 4.

To proceed with the calibration of the hyperparameters in the first-order marginal distribution, consider  $(1,0,0)^T$  as the unit vector defining the symmetry class. The stochastic elasticity matrix can then be expressed in terms of Walpole components as

$$[C] = \begin{bmatrix} M_1 & \frac{\sqrt{2}M_3}{2} & \frac{\sqrt{2}M_3}{2} & 0 & 0 & 0\\ \frac{\sqrt{2}M_3}{2} & \frac{M_2}{2} + \frac{M_4}{2} & \frac{M_2}{2} - \frac{M_4}{2} & 0 & 0 & 0\\ \frac{\sqrt{2}M_3}{2} & \frac{M_2}{2} - \frac{M_4}{2} & \frac{M_2}{2} + \frac{M_4}{2} & 0 & 0 & 0\\ 0 & 0 & 0 & \frac{M_4}{2} & 0 & 0\\ 0 & 0 & 0 & 0 & \frac{M_5}{2} & 0\\ 0 & 0 & 0 & 0 & 0 & \frac{M_5}{2} \end{bmatrix},$$
(54)

or equivalently as  $[C] = [S]^{-1}$ , where [S] is the stochastic compliance matrix given in terms of so-called (stochastic) engineering constants:

$$[S] = \begin{bmatrix} \frac{1}{E_{\ell}} & -\frac{v_{\ell t}}{E_{\ell}} & -\frac{v_{\ell t}}{E_{\ell}} & 0 & 0 & 0\\ -\frac{v_{\ell t}}{E_{\ell}} & \frac{1}{E_{t}} & -\frac{v_{t}}{E_{t}} & 0 & 0 & 0\\ -\frac{v_{\ell t}}{E_{\ell}} & -\frac{v_{t}}{E_{t}} & \frac{1}{E_{t}} & 0 & 0 & 0\\ -\frac{v_{\ell t}}{E_{\ell}} & -\frac{v_{t}}{E_{t}} & \frac{1}{E_{t}} & 0 & 0 & 0\\ 0 & 0 & 0 & \frac{2(1+v_{\ell})}{E_{\ell}} & 0 & 0\\ 0 & 0 & 0 & 0 & \frac{1}{G_{\ell}} & 0\\ 0 & 0 & 0 & 0 & 0 & \frac{1}{G_{\ell}} \end{bmatrix},$$
 (55)

where  $G_{\ell}$  is the stochastic horizontal shear modulus,  $v_{\ell t}$  and  $v_t$  are the stochastic out-of-plane and in-plane Poisson ratios. Recall that  $E_{\ell}$ and  $E_t$  are the stochastic horizontal and transverse Young's moduli. Imposing almost sure equality between the two forms then yields

$$E_{\ell} = -\frac{M_3^2 - M_1 M_2}{M_2} \,, \tag{56}$$

$$E_t = -\frac{2 M_4 \left(M_3^2 - M_1 M_2\right)}{-M_3^2 + M_1 M_2 + M_1 M_4},$$
(57)

$$G_{\ell} = \frac{M_5}{2} \,, \tag{58}$$

$$v_{\ell t} = \frac{\sqrt{2} \, M_3}{2 \, M_2} \,, \tag{59}$$

$$v_t = -\frac{M_3^2 - M_1 M_2 + M_1 M_4}{-M_3^2 + M_1 M_2 + M_1 M_4}.$$
 (60)

$$M_1 = \frac{E_{\ell}^2 v_t - E_{\ell}^2}{2 E_t v_{\ell 1}^2 - E_{\ell} + E_{\ell} v_t},$$
(61)

$$M_2 = -\frac{E_{\ell} E_t}{2 E_t v_{\ell t}^2 - E_{\ell} + E_{\ell} v_t},$$
(62)

$$M_3 = -\frac{\sqrt{2} E_{\ell} E_{t} \nu_{\ell t}}{2 E_{t} \nu_{\ell t}^{2} - E_{\ell} + E_{\ell} \nu_{t}},$$
(63)

$$M_4 = \frac{E_t}{v_t + 1},\tag{64}$$

$$M_5 = 2G_\ell. (65)$$

These relationships show the nonlinearities arising from the transformation from the Walpole form to the form expressed with engineering constants (note that in the above equations, spatial indexation was dropped to simplify notation). This implies that statistical moments estimated on the engineering constants  $E_{\ell}$  and  $E_{t}$  cannot be used to estimate the corresponding moments (such as means) for the Walpole components. Given that the available data are limited, and on the account of the above equations, identification of hyperparameters for  $M_5$ is not pursued and we consider the calibration of the hyperparameters associated with  $M_1$ ,  $M_2$ ,  $M_3$ , and  $M_4$  (which are related to  $E_\ell$  and  $E_t$ ) only. Let  $\underline{E}_\ell$  and  $\underline{E}_t$  denote the mean values of the horizontal and vertical Young's moduli. In addition, it is assumed that the mean values for the Poisson coefficients are such that  $v_{\ell} = v_{\ell t} = 0.3$  (see Li et al. (2020)). We then define the mean values for the considered Walpole coefficients as

$$\underline{M}_{1} = \frac{\underline{E}_{\ell}^{2} \nu_{t} - \underline{E}_{\ell}^{2}}{2 \underline{E}_{t} \nu_{\ell t}^{2} - \underline{E}_{\ell} + \underline{E}_{\ell} \nu_{t}}, \qquad (66)$$

$$\underline{M}_{2} = -\frac{\underline{E}_{\ell} \underline{E}_{t}}{2 \underline{E}_{t} \nu_{\ell t}^{2} - \underline{E}_{\ell} + \underline{E}_{\ell} \nu_{t}}, \qquad (67)$$

$$\underline{M}_2 = -\frac{\underline{E}_{\ell} \, \underline{E}_t}{2 \, E_{\ell} \, V_{\ell}^2 - E_{\ell} + E_{\ell} \, V_{\ell}},\tag{67}$$

$$\underline{M}_{3} = -\frac{\sqrt{2} \underline{E}_{\ell} \underline{E}_{t} \underline{\nu}_{\ell t}}{2 \underline{E}_{t} \underline{\nu}_{\ell t}^{2} - \underline{E}_{\ell} + \underline{E}_{\ell} \underline{\nu}_{t}}, \tag{68}$$

$$\underline{M}_4 = \frac{\underline{E}_t}{\nu_* + 1} \,. \tag{69}$$

The above equations constitute approximations, due to the nonlinear nature of the mappings, and are introduced to reduce the size of the calibration problem. In this setting, the only parameters that remain to be identified are the coefficients of variation  $\delta_{[N]}$  and  $\delta_{M_A}$ . Here we rely on the maximum likelihood method, using a regular mesh in the search space. Once samples of the Walpole are generated for given values of the coefficients, using the stochastic model presented in Section 3.2, the associated samples of the horizontal and vertical Young's moduli are computed and used in a kernel density estimator. It is found that optimal values given the experimental dataset are given by

$$\delta_{[N]} = 0.12, \delta_{M_A} = 0.08. \tag{70}$$

The kernel density estimators corresponding to these two values, together with the experimental results are shown in Fig. 5. These figures illustrate good qualitative agreement between the experimental data and the calibrated models, and show that the experimental distributions associated with the two elastic moduli present skewness coefficients with opposite signs. Note, however, that the number of experimental samples is not large enough to ensure complete convergence in the estimators (and therefore, to draw firm conclusions regarding, e.g., skewness).

#### 4.1.2. Stochastic plasticity model

Here, we address the calibration of the hyperparameters in the stochastic model for the random field  $\{P(x) = (U(x), W(x))^T, x \in \Omega\},\$ presented in Section 3.3. Following the description of the experiments provided in Section 2.2, the database is composed of 4 samples for each field, each of which is associated with one realization of the box and a specific face on the latter (see Fig. 2). For a given face, 8 samples are collected with a space step size of 10 [mm]. The realizations thus obtained on the two boxes for restrictions of the random fields  $\{U(x), x \in \Omega\}$  and  $\{W(x), x \in \Omega\}$  are shown in Figs. 6 and 7. More specifically, we consider:

- the restrictions  $\{U(x_1, L_{12}/2, L_3/2), x_1 \in \Omega_1\}$  and  $\{U(-L_{12}/2, x_2, x_3), x_1 \in \Omega_1\}$  $L_3/2$ ),  $x_2 \in \Omega_2$ } of random field  $\{U(x), x \in \Omega\}$ , characterized on Faces 3 and 4; and
- the restrictions  $\{W(0, -L_{12}/2, x_3), x_3 \in \Omega_3\}$  and  $\{W(L_{12}/2, 0, x_3),$  $x_3 \in \Omega_3$  of random field  $\{W(x), x \in \Omega\}$ , characterized on Faces

Substantial variability is observed for both fields, following the fluctuations observed in Tables 1 and 2 (see Eqs. (39) and (43) as well). In the following, we further simplify notation and use  $\{U(x_1), x_1 \in \Omega_1\}$ ,  $\{U(x_2), x_2 \in \Omega_2\}$ , and  $\{W(x_3), x_3 \in \Omega_3\}$  to denote the aforementioned restrictions.

Given that the directional yield stresses were not characterized jointly, we select  $\rho_{UW} = 0$  in accordance with information theory and hence, the two non-Gaussian fields are written as

$$P_1(x_i) = \left(F_{\mathcal{G}(1/\delta_U^2,\underline{u}\delta_U^2)}^{-1} \circ F_{\mathcal{N}(0,1)}\right) \left(\Xi_1(x_i)\right)\,,\quad \forall x_i \in \Omega_i\,,\quad i=1,2\,, \tag{71}$$

$$P_2(x_3) = \left(F_{\mathcal{G}(1/\delta_W^2, \underline{w}\delta_W^2)}^{-1} \circ F_{\mathcal{N}(0,1)}\right) \left(\Xi_2(x_3)\right), \quad \forall x_3 \in \Omega_3, \tag{72}$$

where the mean values and coefficients of variation are estimated as

$$u = 7.8929, \quad w = 14.6350,$$
 (73)

in [GPa<sup>-2</sup>], and

$$\delta_U = 0.0422, \quad \delta_W = 0.0736,$$
 (74)

respectively. Based on the database, we will seek plausible values for the correlation lengths of the latent Gaussian fields  $\Xi_1$  and  $\Xi_2$  in the next section.

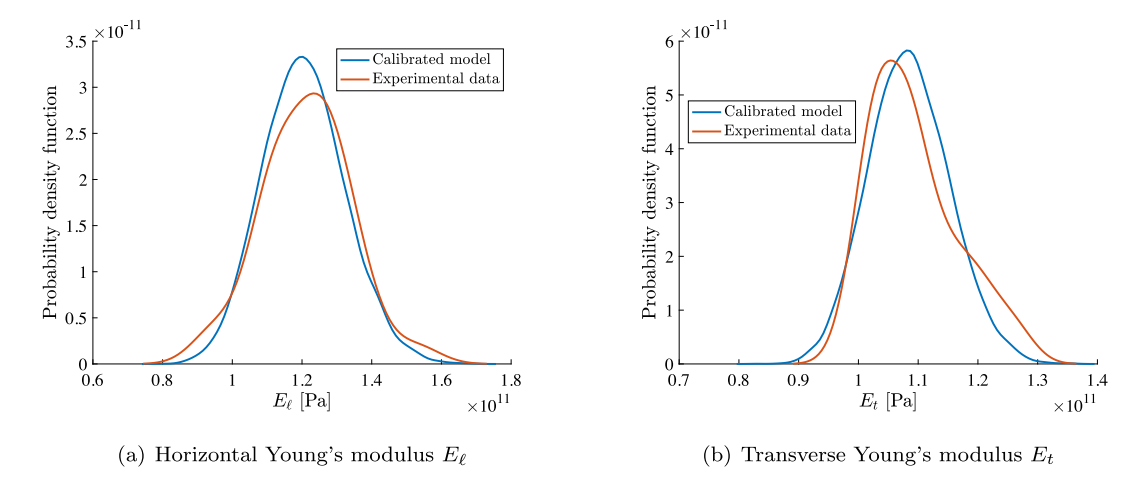


Fig. 5. Kernel density estimators of the probability density functions for the horizontal and vertical Young's moduli obtained from the calibrated model and from experiments.

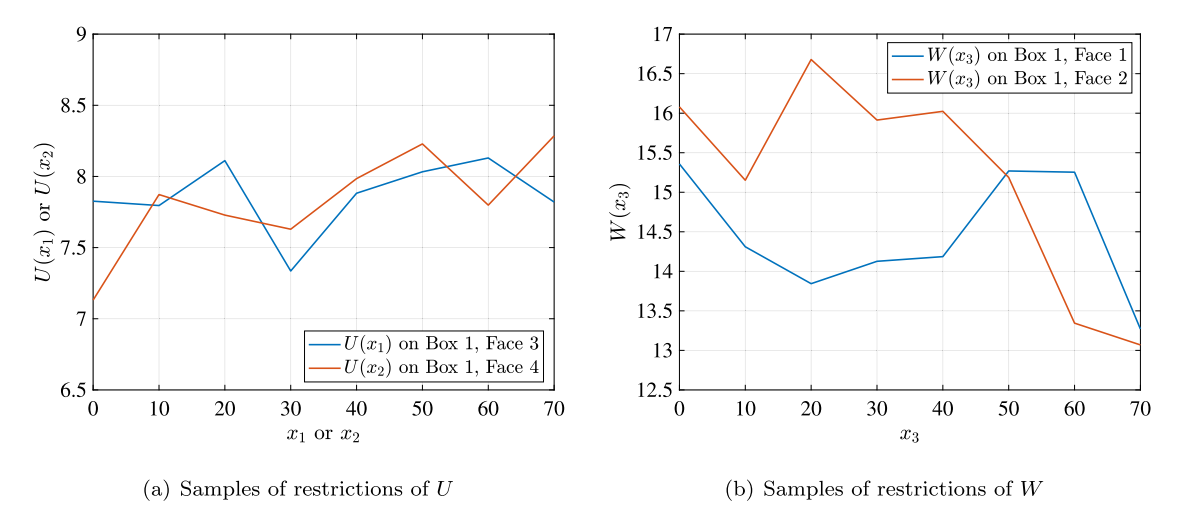


Fig. 6. Realizations of restrictions  $\{U(x_1,L_{12}/2,L_3/2),x_1\in\Omega_1\}$  and  $\{U(-L_{12}/2,x_2,L_3/2),x_2\in\Omega_2\}$  (left panel), and  $\{W(0,-L_{12}/2,x_3),x_3\in\Omega_3\}$  and  $\{W(L_{12}/2,0,x_3),x_3\in\Omega_3\}$  (right panel) on Box 1 (in [GPa<sup>-2</sup>]).

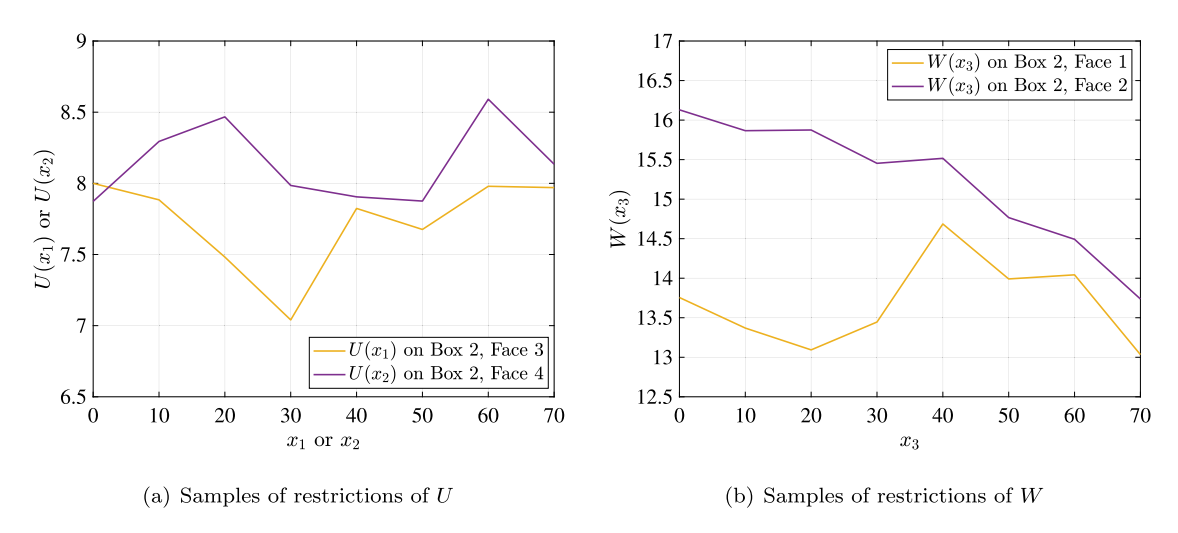


Fig. 7. Realizations of restrictions  $\{U(x_1,L_{12}/2,L_3/2), x_1 \in \Omega_1\}$  and  $\{U(-L_{12}/2,x_2,L_3/2), x_2 \in \Omega_2\}$  (left panel), and  $\{W(0,-L_{12}/2,x_3), x_3 \in \Omega_3\}$  and  $\{W(L_{12}/2,0,x_3), x_3 \in \Omega_3\}$  (right panel) on Box 2 (in [GPa<sup>-2</sup>]).

#### 4.2. Calibration of the spatial correlation length

#### 4.2.1. Strategy

In order to partially calibrate the correlation lengths, the inverse translation model is considered:

$$\Xi(\mathbf{x}) = \mathcal{T}^{-1}(\mathbf{P}(\mathbf{x})), \quad \forall \, \mathbf{x} \in \Omega, \tag{75}$$

Let  $\overline{L}_i^{(k)}$ ,  $1 \le k \le 2$  be the upper bound on the correlation length associated with the kth component  $\{\Xi_k(x_i), x_i \in \Omega_i\}$  of  $\{\Xi(x_i), x_i \in \Omega_i\}$ . Recall that in the considered experimental setting:

- Samples of  $\bar{\sigma}_{zz}$  are characterized along  $\Omega_1$  and  $\Omega_2$ , and can thus be used to compute samples of the restrictions  $\{U(x_1), x_1 \in \Omega_1\}$  and  $\{U(x_2), x_2 \in \Omega_2\}$ ; see Eq. (39). Using Eq. (75) and owing to the postulated invariance in the (x-y) plane, these samples can be used to obtain and merge the samples of the restrictions  $\{\Xi_1(x_1), x_1 \in \Omega_1\}$  and  $\{\Xi_1(x_2), x_2 \in \Omega_2\}$  (with the transport map identified in Section 4.1.2).
- Similarly, samples of  $\bar{\sigma}_{xx}$  and  $\bar{\sigma}_{yy}$  are characterized along  $\Omega_3$ , and allow for the estimation of the samples of  $\{W(x_3), x_3 \in \Omega_3\}$ ; see Eq. (43), with Eq. (39). These samples can, in turn, be used to compute the samples of  $\{\mathcal{Z}_2(x_3), x_3 \in \Omega_3\}$  (merging samples collected on all faces corresponding to  $\Omega_1$  and  $\Omega_2$ ), using the results calibrated in Section 4.1.2.

Let  $\xi^{\exp,ik}$  be the (deterministic) vector gathering the experimental realization of  $\{\Xi_k(x_i), x_i \in \Omega_i\}$  at the experimentally sampled points. Let  $\{\Xi^{\mathrm{mod}}(x_i), x_i \in \Omega_i\}$  be a scalar-valued, centered Matérn Gaussian random field, with  $\alpha=1/2$  and correlation length L. This model is chosen for the sake of calibration, given that the latent Gaussian fields will effectively be simulated with the SPDE approach recalled in Section 3.1.1. Similarly, let  $\Xi^{\mathrm{mod}}(L)$  be the Gaussian random vector gathering the values of  $\{\Xi^{\mathrm{mod}}(x_i), x_i \in \Omega_i\}$  at the sampled points. This random vector is here interpreted as a function of L for calibration purposes. Consider

$$\boldsymbol{\Xi}^{\text{mod}}(L) = \begin{bmatrix} \boldsymbol{\Xi}_{1}^{\text{mod}}(L) \\ \boldsymbol{\Xi}_{2}^{\text{mod}}(L) \end{bmatrix}, \tag{76}$$

where  $\Xi_1^{\mathrm{mod}}(L)$  and  $\Xi_2^{\mathrm{mod}}(L)$  are random vectors of lengths  $(N_p-N_f)$  and  $N_f$ , respectively, where  $N_p$  denotes the number of points where samples are collected, and  $N_f$  is a user-specified number of points. Notice that the above partition is not necessarily contiguous and ordered in space. Let

$$\boldsymbol{\xi}^{\exp,ik} = \begin{bmatrix} \boldsymbol{\xi}_1^{\exp,ik} \\ \boldsymbol{\xi}_2^{\exp,ik} \end{bmatrix}$$
 (77)

be the partition of experimental data, defined as in Eq. (76). Since  $\mathbf{\Xi}^{\mathrm{mod}}(L)$  is Gaussian, we have that  $\mathbf{\Xi}_1^{\mathrm{mod}}(L)|\mathbf{\Xi}_2^{\mathrm{mod}}(L)=\boldsymbol{\xi}_2^{\mathrm{exp},lk}$  is distributed according to

$$\mathcal{N}([\Sigma_{12}^{\text{mod}}(L)][\Sigma_{22}^{\text{mod}}(L)]^{-1}\xi_{2}^{\text{exp},ik}, [\Sigma_{11}^{\text{mod}}(L)] - [\Sigma_{12}^{\text{mod}}(L)][\Sigma_{22}^{\text{mod}}(L)]^{-1}[\Sigma_{21}^{\text{mod}}(L)]),$$
(78)

where  ${\mathcal N}$  is the Gaussian distribution and the covariance matrix of  ${\boldsymbol \Xi}^{\rm mod}(L)$  is given by

$$[\Sigma^{\text{mod}}(L)] = \begin{bmatrix} [\Sigma_{11}^{\text{mod}}(L)] & [\Sigma_{12}^{\text{mod}}(L)] \\ [\Sigma_{21}^{\text{mod}}(L)] & [\Sigma_{22}^{\text{mod}}(L)] \end{bmatrix}, \tag{79}$$

with a block structure induced by the above partition (see Eq. (76)).

An upper bound for the correlation length  $L_i^{(k)}$  can then be identified by the maximum likelihood method:

$$\overline{L}_{i}^{(k)} = \operatorname{argmax}_{L>0} \prod_{j=1}^{N_{p}-N_{f}} f_{\Xi_{1,j}^{\operatorname{mod}}(L)}(\xi_{1,j}^{\operatorname{exp},ik}), \tag{80}$$

where

•  $\xi_{1,j}^{\exp,ik}$  is the *j*th component of  $\xi_1^{\exp,ik}$ ; and

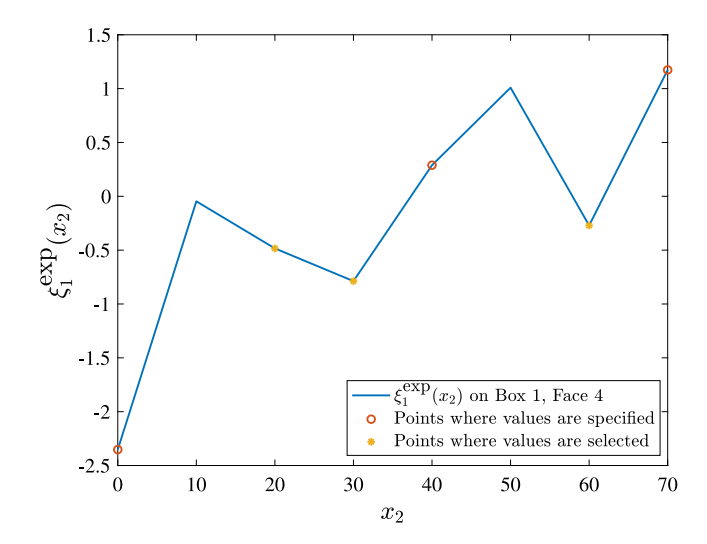


Fig. 8. Realization of the latent Gaussian random field  $\{\mathcal{Z}_1(x_2), x_2 \in \Omega_2\}$  obtained by pulling back the sample of the restriction  $\{U(-L_{12}/2, x_2, L_3/2), x_2 \in \Omega_2\}$  on Box 1 (see Fig. 6). Here, red and orange circular markers indicate points where conditioning is performed and where the likelihood function is computed. (For interpretation of the references to color in this figure legend, the reader is referred to the web version of this article.)

• the probability density function  $f_{\Xi_{1,j}^{\mathrm{mod}}(L)}$  defining the jth component of  $\Xi_{1}^{\mathrm{mod}}(L)$  is obtained by the Monte Carlo approach and nonparametric kernel estimation (for a given L). In the applications presented below, a QR factorization technique was employed for sampling purposes, to ensure stability over the considered range of correlation lengths, and the estimators were computed using 10,000 independent samples.

The rationale behind the above strategy is that values of L that are larger than the sought-after correlation length lead to low likelihood values (with a monotonic decrease trend), since spatial variations cannot be captured accurately. On the other hand, the likelihood function exhibits small fluctuations and/or a plateau for values that are smaller than the most plausible value of the correlation length (which supports the consideration of an upper bound, rather than a point estimate, for the considered correlation length).

In practice, the choice of the  $N_f$  points upon which conditioning is performed is guided by the local monotonicity of the experimental samples. In particular, non-negligible variations should exist around the  $N_f$  selected points, so that the likelihood estimator becomes informative.

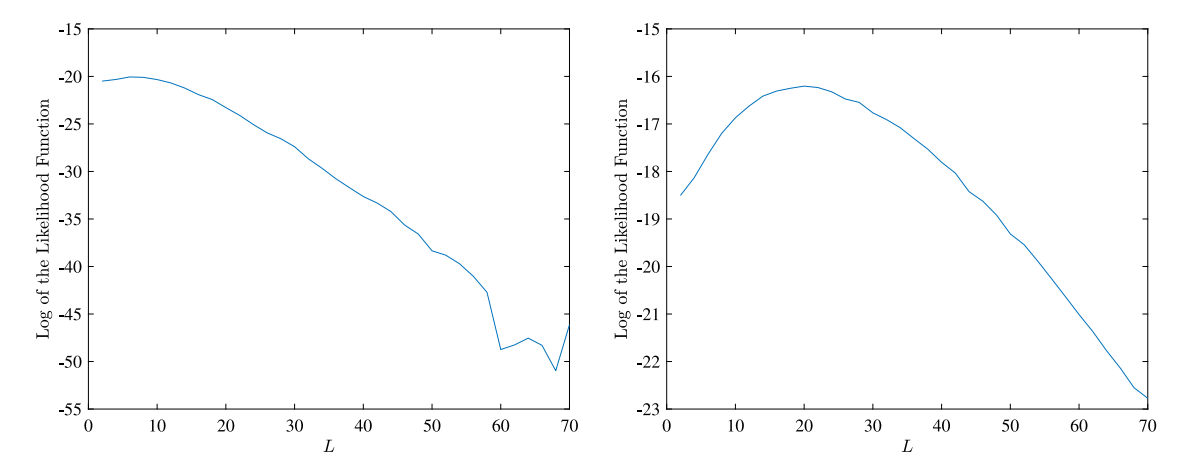
# 4.2.2. Results

One experimental sample of the latent Gaussian random field  $\{\Xi_1(x_2), x_2 \in \Omega_2\}$  is shown in Fig. 8, together with the definition of the points used for conditioning and estimating the likelihood function.

Figs. 9(a) and 9(b) show the evolution of the likelihood functions in terms of the correlation length  $\ell$ .

Possible values for the correlation length along  $x_1$  and  $x_2$ , associated with the random field U (and the directional yield stress  $\bar{\sigma}_{zz}$ ), lie within the range 5–8 [mm], while plausible values for the correlation length along  $x_3$ , associated with the random field W (and the directional yield stresses  $\bar{\sigma}_{xx}$  and  $\bar{\sigma}_{yy}$ ), are between 18 and 22 [mm].

While the above ranges may not be compared with one another without caution, given that they were identified on two different random fields (and with a very limited number of samples), they tend to suggest pronounced anisotropy in the correlation structure (as induced by processing conditions).



(a) Plot of the log-likelihood function for the restriction of U (b) Plot of the log-likelihood function for the restriction of W

Fig. 9. Plot of the log-likelihood function as a function of the correlation length  $\ell$  in the Matérn covariance function (with  $\nu=\frac{1}{2}$ ) for the restriction of U (left) and W (right).

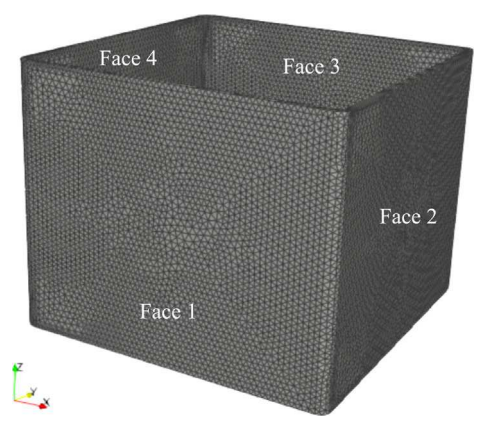


Fig. 10. Finite element mesh of the CAD model for the box.

## 4.3. Simulations of the calibrated model

In this section, we perform sampling of the calibrated stochastic model to exemplify the structure of the directional yield stress fields. Since the dataset does not allow for the calibration of all hyperparameters, and specifically for the estimation of the correlation lengths along  $x_3$  for  $\bar{\sigma}_{zz}$  and along  $x_1$  and  $x_2$  for  $\bar{\sigma}_{xx}$  and  $\bar{\sigma}_{yy}$ , we assume that the correlation lengths, while direction-dependent, are the same for all directional yield stresses. We thus retain the following values for the correlation lengths:

$$L_1^{(k)} = L_2^{(k)} = 6, \quad L_3^{(k)} = 20,$$
 (81)

in [mm], regardless of the latent Gaussian field (that is,  $\forall k \in \{1,2\}$ ).

# 4.3.1. Construction of the orientation fields

In this application, the directional fields are computed as follows. First, an orientation field, here taken as  $e^{(2)}$ , is computed by solving the Laplace problem (see Eq. (7)) with  $\Psi=0$  and  $\Psi=1$  on the inner and outer surface of the box, respectively. The vertical directional field is then defined as  $e^{(3)}=(0,0,1)^T$ , and the last field  $e^{(1)}$  is finally computed by taking the cross product between  $e^{(2)}$  and  $e^{(3)}$ .

We consider a discretization of the domain using 73,472 linear tetrahedral elements (24,401 nodes), shown in Fig. 10.

Since the mesh is too dense to visualize the directional fields over the whole domain, nodes were uniformly selected over the domain and plots of the directional fields  $e^{(1)}$  and  $e^{(2)}$  are shown in Fig. 11.

#### 4.3.2. Generating samples of the calibrated plasticity model

Following the results presented in the previous sections, the stochastic fields of plasticity parameters can be simulated by defining the latent Gaussian fields through the SPDE approach with the diffusion field (see Eq. (5))

$$[H^{(k)}(x)] = \sum_{i=1}^{3} \lambda_{i}^{(k)} e^{(i)}(x) \otimes e^{(i)}(x), \quad \forall x \in \Omega,$$
(82)

where  $\{\lambda_i^{(k)}\}$  satisfy

$$L_i^{(k)} = \frac{\sqrt{\lambda_i^{(k)}}}{\kappa} \,, \tag{83}$$

with  $\kappa=1$  and L=(6,6,20) (in [mm]), regardless of the plasticity parameter. It should be noticed that it is implicitly assumed that the plasticity parameters exhibit the same correlation lengths along each direction—an assumption that may be relaxed, should further experiments be conducted to characterize all correlation lengths.

Samples of the non-Gaussian fields U and  $\sigma_{zz}$  are shown in Fig. 12. Samples of the non-Gaussian fields W and  $\sigma_{xx}$  are shown in Fig. 13.

#### 5. Conclusion

In this work, the construction and partial identification of a stochastic elasto-plastic constitutive model were addressed. The model accounts for the anisotropy observed in physical tensile experiments on both the elastic and plastic response (specifically, on the horizontal and vertical Young's moduli, as well as on the directional yield strengths). Variability ranging from three to twelve percent is observed, depending on the property. An information-theoretic stochastic framework was leveraged to derive admissible probabilistic models involving a low-dimensional parameterization. These representations were subsequently calibrated utilizing the experimental results, using statistical estimators for the hyperparameters in the transport maps and a maximum-likelihood-based methodology to estimate spatial correlation lengths. Good quantitative agreement is observed in terms of first-order marginal distributions. Results related to the covariance structure suggest strong anisotropy as well. While these findings require additional experiments, given the anisotropy in both the yield criterion and covariance structure, the overall approach paves the way for simulating elasticity and plasticity material parameters on complex geometries produced by additive manufacturing.

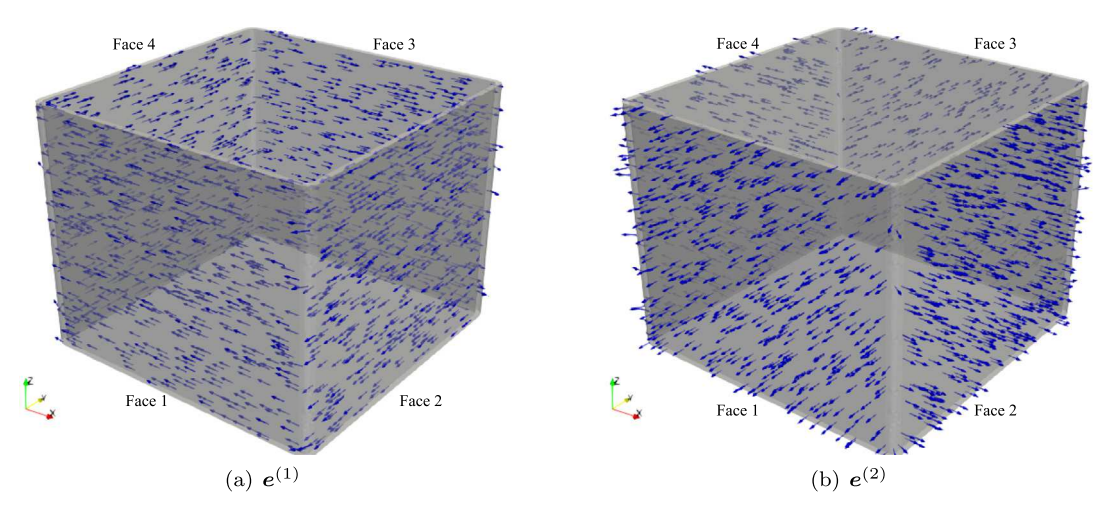


**Fig. 11.** Orientation fields  $e^{(1)}$  and  $e^{(2)}$  for the box model.

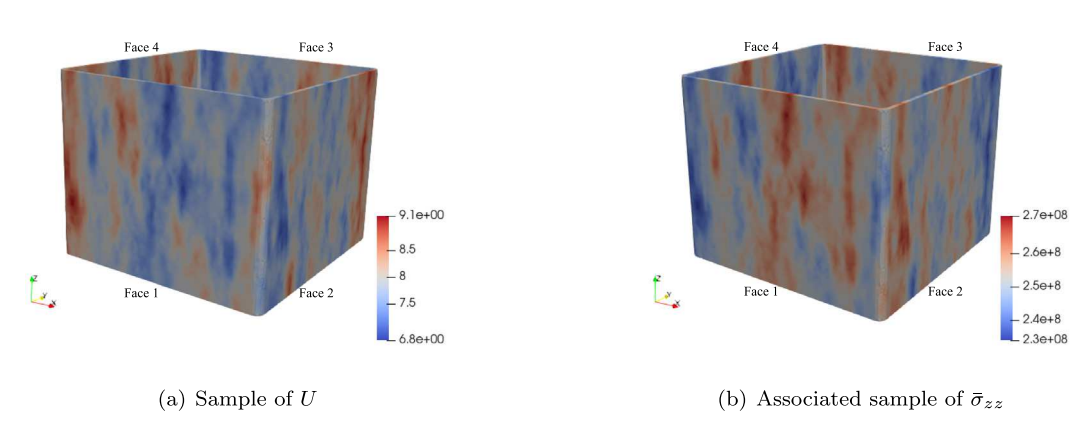


Fig. 12. Sample of U in [GPa<sup>-2</sup>] and associated sample of  $\bar{\sigma}_{zz}$  in [Pa].

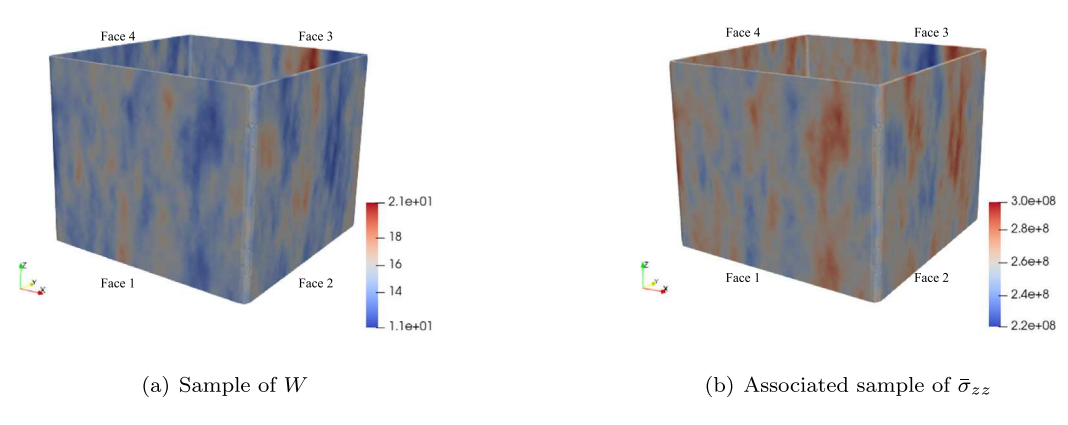


Fig. 13. Sample of W in [GPa<sup>-2</sup>] and associated sample of  $\bar{\sigma}_{xx}$  in [Pa].

# Declaration of competing interest

The authors declare the following financial interests/personal relationships which may be considered as potential competing interests: Johann Guilleminot reports financial support was provided by National Science Foundation.

# Data availability

The authors can share data after such a request has been made for the data and the request has been cleared for release by their respective institutions

# Acknowledgments

The work of S.C. was supported by the National Science Foundation, Division of Civil, Mechanical and Manufacturing Innovation, under award CMMI-1942928. The work of J.G. was partially supported by the U.S. National Research Laboratory (US NRL) under contract N0017321P1059, as well as by the National Science Foundation, Division of Civil, Mechanical and Manufacturing Innovation, under award CMMI-1942928. The work of A.I., J.M., J.S., and J.T. was supported by the Office of Naval Research via U.S. Naval Research Laboratory's core funding. This support is gratefully acknowledged.

#### References

- Acton, Katherine A., Baxter, Sarah C., 2018. Characterization of random composite properties based on statistical volume element partitioning. J. Eng. Mech. 144 (2), 04017168
- Arendt, Paul D., Apley, Daniel W., Chen, Wei, 2012. Quantification of model uncertainty: Calibration, model discrepancy, and identifiability. J. Mech. Des. 134 (10).
- Bolin, D., Kirchner, K., 2020. The rational SPDE approach for Gaussian random fields with general smoothness. J. Comput. Graph. Statist. 29 (2), 274–285.
- Bolin, D., Lindgren, F., 2011. Spatial models generated by nested stochastic partial differential equations, with an application to global ozone mapping. Ann. Appl. Stat. 5 (1), 523–550.
- Bolin, D., Wallin, J., 2020. Multivariate type G Matérn stochastic partial differential equation random fields. J. R. Stat. Soc. Ser. B 82 (1), 215–239.
- Cai, G., Mahadevan, S., 2016. Uncertainty quantification of manufacturing process effects on macroscale material properties. Int. J. Multiscale Comput. Eng. 14 (3).
- Chu, Shanshan, Guilleminot, Johann, 2019. Stochastic multiscale modeling with random fields of material properties defined on nonconvex domains. Mech. Res. Commun. 97, 39–45.
- Chu, S., Guilleminot, J., Kelly, C., Abar, B., Gall, K., 2021. Stochastic modeling and identification of material parameters on structures produced by additive manufacturing. Comput. Methods Appl. Mech. Engrg. 387, 114166.
- Daon, Y., Stadler, G., 2018. Mitigating the influence of the boundary on PDE-based covariance operators. Inverse Probl. Imaging 12 (5), 1083–1102.
- DebRoy, Tarasankar, Wei, H.L., Zuback, J.S., Mukherjee, Tuhin, Elmer, J.W., Milewski, J.O., Beese, Allison Michelle, Wilson-Heid, A. de, De, Amitava, Zhang, Wei, 2018. Additive manufacturing of metallic components-process, structure and properties. Prog. Mater. Sci. 92, 112–224.
- Dunlop, M.M., Stuart, A.M., 2016. The Bayesian formulation of EIT: Analysis and algorithms. Inverse Probl. Imaging 10 (4), 1007–1036.
- Fuglstad, G.-A., Lindgren, F., Simpson, D., Rue, H., 2015. Exploring a new class of nonstationary spatial Gaussian random fields with varying local anisotropy. Statist. Sinica 25 (1), 115–133.
- Grigoriu, M., 1984. Crossings of non-Gaussian translation processes. J. Eng. Mech. 110 (4), 610–620.
- Guilleminot, J., 2020. 12 Modeling non-Gaussian random fields of material properties in multiscale mechanics of materials. In: Wang, Yan, McDowell, David L. (Eds.), Uncertainty Quantification in Multiscale Materials Modeling. In: Elsevier Series in Mechanics of Advanced Materials, Woodhead Publishing, pp. 385–420.
- Guilleminot, J., Asadpoure, A., Tootkaboni, M., 2019. Topology optimization under topologically dependent material uncertainties. Struct. Multidiscip. Optim. 60, 1283–1287.
- Guo, Nannan, Leu, Ming C., 2013. Additive manufacturing: Technology, applications and research needs. Front. Mech. Eng. 8, 215–243.
- Hu, Z., Mahadevan, S., 2017. Uncertainty quantification and management in additive manufacturing: current status, needs, and opportunities. Int. J. Adv. Manuf. Technol. 93 (5), 2855–2874.
- Huang, Yong, Leu, Ming C., Mazumder, Jyoti, Donmez, Alkan, 2015. Additive manufacturing: Current state, future potential, gaps and needs, and recommendations. J. Manuf. Sci. Eng. 137 (1).
- Hun, Darith-Anthony, Guilleminot, Johann, Yvonnet, Julien, Bornert, Michel, 2019. Stochastic multiscale modeling of crack propagation in random heterogeneous media. Internat. J. Numer. Methods Engrg. 119 (13), 1325–1344.
- Ian Gibson, Ian Gibson, 2015. Additive Manufacturing Technologies 3D Printing, Rapid Prototyping, and Direct Digital Manufacturing. Springer.
- Iliopoulos, A., Michopoulos, J.G., Birnbaum, A., Steuben, J.C., Stewart, C., Rowenhorst, D., 2020a. Structural performance modeling of additively manufactured parts under process-induced inhomogeneity and property anisotropy. In: ASTM ICAM Virtual Conference.
- Iliopoulos, A.P., Thomas, J.P., Steuben, J.C., Saunders, R., Michopoulos, J.G., Bagchi, A., Birnbaum, A.J., 2020b. Statistical analysis of tensile tests performed on 316L specimens manufactured by directed energy deposition. In: International Design Engineering Technical Conferences and Computers and Information in Engineering Conference, Vol. 83983. American Society of Mechanical Engineers, V009T09A024.
- Jaynes, E.T., 1957a. Information theory and stastitical mechanics II. Phys. Rev. 108 (2), 171–190.
- Jaynes, E.T., 1957b. Information theory and statistical mechanics I. Phys. Rev. 106 (4), 620–630.
- Kamiński, Marcin M., 2021. On Shannon entropy computations in selected plasticity problems. Internat. J. Numer. Methods Engrg. 122 (18), 5128–5143.
- Kennedy, Marc C., O'Hagan, Anthony, 2001. Bayesian calibration of computer models.
  J. R. Stat. Soc. Ser. B Stat. Methodol. 63 (3), 425–464.
- Khristenko, U., Scarabosio, L., Swierczynski, P., Ullmann, E., Wohlmuth, B., 2019. Analysis of boundary effects on PDE-based sampling of Whittle-Matérn random fields. SIAM/ASA J. Uncertain. Quantif. 7 (3), 948–974.

- Kotha, S., Ozturk, D., Smarslok, B., Ghosh, S., 2020. Uncertainty quantified parametrically homogenized constitutive models for microstructure-integrated structural simulations. Integr. Mater. Manuf. Innov. 9 (4), 322–338.
- Li, X., Roth, C.C., Tancogne-Dejean, T., Mohr, D., 2020. Rate-and temperature-dependent plasticity of additively manufactured stainless steel 316L: Characterization, modeling and application to crushing of shell-lattices. Int. J. Impact Eng. 145. 103671.
- Lindgren, Finn, Bolin, David, Rue, Håvard, 2022. The SPDE approach for Gaussian and non-Gaussian fields: 10 years and still running. Spatial Stat. 50, 100599, Special Issue: The Impact of Spatial Statistics.
- Lindgren, F., Rue, H., Lindström, J., 2011. An explicit link between Gaussian fields and Gaussian Markov random fields: The stochastic partial differential equation approach. J. R. Stat. Soc. Ser. B Stat. Methodol. 73 (4), 423–498.
- Mahadevan, Sankaran, Nath, Paromita, Hu, Zhen, 2022. Uncertainty Quantification for Additive Manufacturing Process Improvement: Recent Advances. ASCE-ASME J. Risk Uncert. Engrg. Sys. B Mech. Engrg. 8 (1).
- Maloth, T., Ozturk, D., Hommer, G.M., Pilchak, A.L., Stebner, A.P., Ghosh, S., 2020.
  Multiscale modeling of cruciform dwell tests with the uncertainty-quantified parametrically homogenized constitutive model. Acta Mater. 200, 893–907.
- Mejia, A.F., Yue, Y.R., Bolin, D., Lindgren, F., Lindquist, M.A., 2020. A Bayesian general linear modeling approach to cortical surface fMRI data analysis. J. Amer. Statist. Assoc. 115 (530), 501–520.
- Nath, P., Hu, Z., Mahadevan, S., 2017. Multi-level uncertainty quantification in additive manufacturing. In: Solid Freeform Fabrication 2017: Proceedings of the 28th Annual International Solid Freeform Fabrication Symposium – an Additive Manufacturing Conference. pp. 922–937.
- Nouy, A., Soize, C., 2014. Random field representations for stochastic elliptic boundary value problems and statistical inverse problems. European J. Appl. Math. 25 (3), 339–373.
- Ostoja-Starzewski, Martin, 2007. Microstructural Randomness and Scaling in Mechanics of Materials. Chapman & Hall/CRC Press.
- Ozturk, D., Kotha, S., Ghosh, S., 2021. An uncertainty quantification framework for multiscale parametrically homogenized constitutive models (PHCMs) of polycrystalline Ti alloys. J. Mech. Phys. Solids 148, 104294.
- Pokusiński, Bartłomiej, Kamiński, Marcin, 2023. Numerical convergence and error analysis for the truncated iterative generalized stochastic perturbation-based finite element method. Comput. Methods Appl. Mech. Engrg. 410, 115993.
- Prabhune, Bhagyashree C., Suresh, Krishnan, 2020. A fast matrix-free elasto-plastic solver for predicting residual stresses in additive manufacturing. Comput. Aided Des 123 102829
- Roininen, L., Girolami, M., Lasanen, S., Markkanen, M., 2019. Hyperpriors for Matérn fields with applications in Bayesian inversion. Inverse Probl. Imaging 13 (1), 1–29.
- Roininen, L., Huttunen, J.M.J., Lasanen, S., 2014. Whittle-Matérn priors for Bayesian statistical inversion with applications in electrical impedance tomography. Inverse Probl. Imaging 8 (2), 561–586.
- Rosa, Francesco, Manzoni, Stefano, Casati, Riccardo, 2018. Damping behavior of 316L lattice structures produced by selective laser melting. Mater. Des. 160, 1010–1018.
- Sames, William J., List, F.A., Pannala, Sreekanth, Dehoff, Ryan R., Babu, Sudarsanam Suresh, 2016. The metallurgy and processing science of metal additive manufacturing. Int. Mater. Rev. 61 (5), 315–360.
- Shannon, C.E., 1948a. A mathematical theory of communication. Bell Syst. Tech. J. 27 (3), 379–423.
- Shannon, C.E., 1948b. A mathematical theory of communication. Bell Syst. Tech. J. 27 (4), 623–656.
- Sidén, P., Eklund, A., Bolin, D., Villani, M., 2017. Fast Bayesian whole-brain fMRI analysis with spatial 3D priors. NeuroImage 146, 211–225.
- Sidén, P., Lindgren, F., Bolin, D., Eklund, A., Villani, M., 2019. Spatial 3D Matérn priors for fast whole-brain fMRI analysis. arXiv.
- Soize, C., 2000. A nonparametric model of random uncertainties for reduced matrix models in structural dynamics. Probab. Eng. Mech. 15 (3), 277–294.
- Soize, C., 2006. Non-Gaussian positive-definite matrix-valued random fields for elliptic stochastic partial differential operators. Comput. Methods Appl. Mech. Engrg. 195 (1) 26-64
- Staber, B., Guilleminot, J., 2017. Stochastic modeling and generation of random fields of elasticity tensors: A unified information-theoretic approach. Comptes Rendus Mécanique 345 (6), 399–416.
- Staber, B., Guilleminot, J., 2018. A random field model for anisotropic strain energy functions and its application for uncertainty quantification in vascular mechanics. Comput. Methods Appl. Mech. Engrg. 333, 94–113.
- Supriyo, G., Mohamad, M., Johnson, L., Elwany, A., Raymundo, A., Allaire, D., 2019. Uncertainty analysis of microsegregation during laser powder bed fusion. Modelling Simul. Mater. Sci. Eng. 27 (3), 034002.
- Supriyo, G., Raiyan, S., Jaylen, J., Karaman, I., Elwany, A., Allaire, D., Arroyave, R., 2020. Statistical modelling of microsegregation in laser powder-bed fusion. Phil. Mag. Lett. 100 (6), 271–282.

- Thompson, James R., Tapia, Richard A., 1990. Nonparametric Function Estimation, Modeling, and Simulation. Society for Industrial and Applied Mathematics.
- Walpole, L.J., 1984. Fourth-rank tensors on the thirty-two crystal classes: Multiplication tables. Proc. R. Soc. Lond. A 391, 149–179.
- Wang, Zhuo, Jiang, Chen, Liu, Pengwei, Yang, Wenhua, Zhao, Ying, Horstemeyer, Mark F., Chen, Long-Qing, Hu, Zhen, Chen, Lei, 2020. Uncertainty quantification and reduction in metal additive manufacturing. npj Comput. Mater. 6 (1), 175.
- Wang, Z., Liu, P., Ji, Y., Mahadevan, S., Horstemeyer, M.F., Hu, Z., Chen, L., Chen, L.-Q., 2019. Uncertainty quantification in metallic additive manufacturing through physics-informed data-driven modeling. J. Miner. Metals Mater. Soc. 71 (8), 2625–2634.
- Weber, G., Pinz, M., Ghosh, S., 2022. Machine learning-enabled self-consistent parametrically-upscaled crystal plasticity model for Ni-based superalloys. Comput. Methods Appl. Mech. Engrg. 115384.
- Whittle, P., 1954. On stationary processes in the plane. Biometrika 41 (3-4), 434-449.Whittle, P., 1963. Stochastic processes in several dimensions. Bull. Int. Stat. Inst. 40, 974-994.